

Check for updates

Sensitive Thermochromic Behavior of InSel, a Highly Anisotropic and Tubular 1D van der Waals Crystal

Dmitri Leo Mesoza Cordova, Yinong Zhou, Griffin M. Milligan, Leo Cheng, Tyler Kerr, Joseph Ziller, Ruqian Wu, and Maxx Q. Arguilla*

Thermochromism, the change in color of a material with temperature, is the fundamental basis of optical thermometry. A longstanding challenge in realizing sensitive optical thermometers for widespread use is identifying materials with pronounced thermometric optical performance in the visible range. Herein, it is demonstrated that single crystals of indium selenium iodide (InSeI), a 1D van der Waals (vdW) solid consisting of weakly bound helical chains, exhibit considerable visible range thermochromism. A strong temperature-dependent optical band edge absorption shift ranging from 450 to 530 nm (2.8 to 2.3 eV) over a 380 K temperature range with an experimental $(dE_{\sigma}/dT)_{max}$ value extracted to be 1.26 \times 10⁻³ eV K⁻¹ is shown. This value lies appreciably above most dense conventional semiconductors in the visible range and is comparable to soft lattice solids. The authors further seek to understand the origin of this unusually sensitive thermochromic behavior and find that it arises from strong electron-phonon interactions and anharmonic phonons that significantly broaden band edges and lower the E_g with increasing temperature. The identification of structural signatures resulting in sensitive thermochromism in 1D vdW crystals opens avenues in discovering low-dimensional solids with strong temperature-dependent optical responses across broad spectral windows, dimensionalities, and size regimes.

1. Introduction

Many optical and electronic properties in crystalline solids are intrinsically tied to changes in temperature. In most cases,

D. L. M. Cordova, G. M. Milligan, L. Cheng, T. Kerr, J. Ziller, M. Q. Arguilla Department of Chemistry

University of California Irvine, CA 92697, USA E-mail: marguill@uci.edu

Y. Zhou, R. Wu

Department of Physics and Astronomy University of California

Irvine, CA 92697, USA

The ORCID identification number(s) for the author(s) of this article can be found under https://doi.org/10.1002/adma.202312597

© 2024 The Authors. Advanced Materials published by Wiley-VCH GmbH. This is an open access article under the terms of the Creative Commons Attribution-NonCommercial-NoDerivs License, which permits use and distribution in any medium, provided the original work is properly cited, the use is non-commercial and no modifications or adaptations are made.

DOI: 10.1002/adma.202312597

emergent physical signatures and unique phase transitions have been recently observed both in bulk crystals and atomically precise van der Waals (vdW) solids down to the few- to single-atom-thickness regime. Beyond these emergent temperature-reliant phenomena, the dependence of the electrical signatures and optical states of a crystalline solid to changes in temperature is one of the fundamental bases for their identification, electronic structure determination, and subsequent device applications. More practically, the ability to measure precise temperature changes has become an integral aspect of several fields relevant to human life, such as pasteurization for food preparation, quality control for manufacturing, diagnostics for healthcare, efficiency optimization for transportation, and environmental monitoring for climate change research.[1-6] Among the recent developments in the precise determination of temperature,^[7] optical thermometric platforms that are based on the temperature-dependent frequency of the spectral properties of a

material to determine temperature are the most promising alternatives to sensitivity-, stability-, size-, and resolution-limited resistance thermometry. [7,8] The advantage of these optical platforms originates from their intrinsic robustness with respect to electromagnetic interference, remote readout, and high sensitivity of optical measurements. [9-11] In addition, given the renewed focus of public and private sectors on nano- and semiconductor technologies, optical thermometers can play a significant role in addressing the emerging need for temperature monitoring of nanoscale processes related to the thermal management of microelectronics, [12] nanomedicine, [13,14] and biomedical imaging. [15,16]

Thermochromism, which is the temperature-dependent change in the color of a material, is the core foundation of many optical thermometers. These colorimetric changes can be reversible or irreversible, and can often be induced by temperature-dependent structural changes such as phase transitions, crystal field variation, ligand geometry distortion, coordination number change, or electronic structure renormalization. [17] Specifically, thermochromism is associated with measurable frequency shifts in the spectral features of the absorbance and reflectance of materials that scale with changes in temperature. This, in



conjunction with robust thermal stability and broadband optical response, are the most desirable properties when selecting materials for photonic and optical thermometers.[18] For thermal metrology applications, reversible thermochromic materials are better suited because they exhibit gradual changes in optical frequencies over a large energy range while manifesting good cyclability. Reversible thermochromic inorganic solids include tetravalent mercury compounds, [19-21] halide perovskites, [22-24] organic-inorganic hybrid compounds, [25-27] and lanthanidedoped phosphors, [28-31] which exhibit subtle changes in the lattice or coordination structure that ultimately alters the electronic structure in a continuous manner. However, many of these materials are not typically optimized for modern scalable optical thermometric applications due to their inherently dense and bulky form factors and their need for laser sources for excitation.

Semiconducting low-dimensional van der Waals (vdW) materials warrant consideration as candidate thermochromics that are also scalable down to the nanoscale since, first, their bandgaps inherently undergoes significant red shifting with increasing temperatures (Varshni effect), albeit in different extents.[32] Typically, covalent and ionic solid state materials require chemical substitution to alter spectral characteristics. [33,34] Second, owing to the weak interactions across the layers, vdW materials offer a higher degree of tunability, since their properties can be modulated through noninvasive and nonchemical routes such as lowering dimensionality via exfoliation, substrate and strain engineering, and heterostructure formation, thus, increasing the number of parameters that can tune the optical properties, such as layer number or thickness, substrate type, and strain percentage.^[35] For instance, the temperature dependence of the MoS2 bandgap is strongly influenced by thickness and substrate strain, which can further shift the bandgap by up to 0.05 eV.[36,37] Third, vdW solids can be exfoliated down to nanoscale units, underscoring the potential of these materials in delivering high spatial resolution thermometers with minute form factors. Despite these promising attributes, thermochromic studies on low-dimensional materials are severely limited, primarily due to the scarcity of vdW solids that are both optically active and temperature-sensitive in the sought-after visible regime for optical thermometry. 1D van der Waals (1D vdW) solids, which consist of covalently bound chains held together by weak van der Waals forces, exhibit diverse optical signatures that range from the far infrared to the visible region.[38,39] Among these phases, the family of III-VI-VII crystals have recently gained attention as building blocks for electronic, optoelectronic, and sensing device applications owing to their chemically modular 1D helical structures, exfoliability, sizeable optical gaps, and predicted spin filtering capabilities.[40,41]

In this report, we investigate thermochromic behavior of the 1D vdW solid, indium selenium iodide (InSeI) (**Figure 1**). Using in situ absorbance spectroscopy, we observe a prominent and consistent red shift of the visible range bandgap energy ($E_{\rm g}$) by \approx 0.45 eV in InSeI single crystals over the temperature range of 93 to 473 K. Least squares fitting of the temperature dependent bandgap data suggests that the systematic red shifting of the $E_{\rm g}$ is predominantly caused by strong electron–phonon coupling, with negligible contributions from temperature-induced lattice

expansion. Further analysis of the Urbach edges shows that band edge broadening arises from dynamic phonon disorder and not static disorder from defects and imperfections. From the single crystal data collected at 83 and 298 K, anomalous band shortening and thermal ellipsoid distortion was observed, suggesting that anharmonic effects are involved in the thermochromism. Temperature-dependent Raman spectroscopy coupled with firstprinciples calculations of the phonon and electronic band structures was utilized to elucidate lattice dynamics and reveal that phonon modes in InSeI are highly anharmonic and likely participate in the renormalization of the bandgap. We highlight that the calculated $(dE_g/dT)_{max}$ value of 1.26×10^{-3} eV K⁻¹ is more sensitive than any reported vdW material in the visible range and is comparable to soft lattice halide perovskites, demonstrating the high thermal sensitivity of the optical properties of InSeI. We anticipate that our realization of pronounced and sensitive thermochromic behavior in 1D vdW solids would open opportunities to explore how the intrinsic anisotropy of these structures can be leveraged toward improving the thermal resolution and expanding the frequency range accessible to optical thermometry applications.

2. Results

2.1. Synthesis and Structural Characterization of InSel Single Crystals

The low- and high-temperature single crystal structures of InSeI were experimentally determined using single-crystal X-ray diffraction (SC-XRD) and subsequent structural refinement at both 83 and 298 K (Table S1, Supporting Information). The refined structures from both temperatures exhibit the $I4_1/a$ space group and are consistent with the lattice constants previously reported.[42] Retention of the unit cell structure upon heating suggests that there are no significant changes in the static crystal structure. The crystal structure of InSeI (Figure 1a) consists of tubule-like helical chains with core layers of indium and selenium atoms surrounded by an outer layer of iodine atoms that run parallel to the c-axis. Each tubule is comprised of $[InSe_3I]_n$ pseudo-tetrahedra that are corner-sharing at the Se atom. Note that we use a "pseudo-tetrahedral" terminology to indicate that In—Se and In—I bond lengths are not equal. Furthermore, for an ideal pseudo-tetrahedral [InSe₃I]_n subunit, there should be three equivalent ∠Se-In-I and ∠Se-In-Se bond angles. However, the bond angles are not equivalent (see Table S2, Supporting Information), indicating that the [InSe₃I]_n subunits are distorted. The tubules pack within the tetragonal unit cell in a primitivelike manner, with each unit cell containing four tubules due to the 4_1 screw axes in the $I4_1/a$ space group. The 4_1 screw axis also imparts helical features into each tubule, resulting in a unit cell that has alternating handedness tubules along the [010] or [100] direction. The outermost layer of each tubule consists of I atoms, which do not form covalent bonds with corresponding atoms in adjacent tubules. Because of the lack of strong interactions between the tubules, InSeI is considered a 1D vdW crystal. SEM images (Figure 1c; Figure S1a, Supporting Information) show that large crystals delaminate or unbundle easily along the long axis and form flexible ribbons/wires, but do not cleave easily perpendicular to the long axis.



a)

Legend

In + Se
Se
SG I4,/a
a = 18.6051(13) Å
c = 10.0813(7) Å

HRTEM

FFT-filtered

FFT-filtered

-[011]

Figure 1. Synthesis and characterization of InSel. a) Crystal structure representation of InSel depicting the weakly bound tubule-like helical chains. The unit cell of InSel is projected along the [001]- (left) and [100]- (right) zone axes. b) Schematic depicting the melt synthesis from elemental precursors. The optical image of large InSel multigrain crystallites on a 1×1 mm grid is highlighted on the right. Note that the contrast difference between the crystals is due to the thickness and uneven lighting and not from variability in crystal quality. c) SEM image and EDS maps of a micromechanically exfoliated InSel crystal. Scale bar: $10 \,\mu\text{m}$. d, left panel) HRTEM image of InSel nanowire with the long axis (c-axis) direction indicated by a white arrow. Scale bar: $5 \, \text{nm}$. (d, middle panel) High-magnification HRTEM and FFT-filtered images of an exfoliated InSel crystals showing the helical motif features as bright regions. Scale bar: $5 \, \text{nm}$. (d, right panel) FFT of the HRTEM image indicating the indexed zone axis (top) and the corresponding \sim [011]-oriented crystal structure model (bottom).

Solids that are comprised of 1D chains held by weak vdW interactions, such as InSeI, often crystallize from the vapor phase as long needle-like crystals that form a radial growth pattern. While suitable for many device applications, these needle-like crystals limit the exposed surface of the crystals and hamper measurements, which require sizeable areas such as in optical thermometry. To this end, we developed a modified melt reaction, which addresses the limitations of high vapor phase precursors such as elemental selenium and iodine. Synthesis of InSeI via melt reaction from elements produced large yellow high-quality crystals with thick and rod-like morphology, sizeable rectangular facets, and high degree of brittleness. The product crystallized with a prismatic crystal habit that is consistent with a tetragonal unit cell. We opted for a synthesis from elements to minimize the formation of potential competing phases that may arise from the solidus line to the left of the InSeI composition in the phase diagram. Schematic diagram of the synthesis appears in Figure 1b. The earliest report of InSeI synthesis originates from the phase diagram study of the InI₃-In₂Se₃ binary system, where InSeI forms as the only stable ternary compound below 499 °C (772.15 K). Based on the phase diagram, a liquid with 1:1:1 (In:Se:I) composition will have a tendency to form other Inrich phases alongside InSeI since the melt does not solidify congruently.^[43] Often, the synthesis of higher order compounds from elements is often plagued by the formation of competing binary phases that is likely due to precursor inhomogeneity, minute temperature fluctuations, and small differences in the formation energies among the phases.^[44]

To improve the homogeneity of the precursor, the In, Se, and I₂ powder mixture was heated with mechanical agitation to form the low temperature Se:I eutectic (Step I in Figure 1b).[45] This process aids in evenly distributing the highly volatile Se and I2 powders within the precursor mixture and prevents the premature loss of these elements during the initial heating ramp up period, which could lead to an off-stoichiometric precursor reservoir. In addition, the top of the ampoule was wrapped in aluminum foil to 1) improve heat retention in this region, 2) induce a small temperature gradient, and 3) subsequently prevent Se and I₂ from prematurely vaporizing (Step II in Figure 1b). This adjustment was done to concentrate the volatile reactants at the bottom of the ampoule during the melt reaction and to avoid any loss of precursor from vapor-phase processes such as deposition to colder regions of the reaction tube. With these synthetic considerations, and after heating the precursor to 500 °C (773.15 K) (Step III in Figure 1b), sizable multigrain solids with yellow coloration (Figure 1b, right; Figure S1b, Supporting Information)



www.auvmat.ue

that is embedded within a silvery-gray boule emerge from the reaction tube postsynthesis. These boules readily separate into large-faceted 1-2 mm long single crystals upon cleavage that are suitable for subsequent spectroscopic characterization. Elemental composition from EDS (Figure S2 and Table S3, Supporting Information) is consistent with the expected 1:1:1 ratio, with a uniform distribution across exfoliated crystals (Figure 1c). To further corroborate the elemental composition, XPS data were collected on ground single crystal samples mounted on carbon tape (Figure \$3, Supporting Information). In addition to the elemental species, we compared the binding energies to similar tetrahedral In-coordinated compounds, InSe and InI₃. [46–49] There are small differences between the binding energies of the elements in In-SeI compared to their counterparts in other tetrahedral In solids, but the elements display the expected trends with respect to their elemental counterparts, based on the oxidation states: In³⁺, Se²⁻, and I⁻. Additionally, there are no other elemental peaks observed in the XPS spectra besides C 1s and O 1s expected from the mounting medium.

To further assess the crystalline quality of InSeI, we collected high-resolution transmission electron microscopy (HRTEM) of InSeI crystals exfoliated via ultrasonication in acetone. Prior to imaging, plasma cleaning was performed on the samples to thin down the nanostructures and expose fresh surfaces. A nanoribbon structure is observed in the HRTEM image in Figure 1d, left. The small width compared to the length highlights the highly exfoliable nature of InSeI to nanometer length scales. Lattice fringes that correspond to the (100) or (010) planes are observed across the nanoribbon. The vertical axis of the nanoribbon corresponds to the c-axis of the InSeI unit cell, highlighting the anisotropy of covalent growth (along c-axis) compared to vdW growth (along a-b plane). Higher magnification image of another representative sample (Figure 1d, middle) emphasizes the helical nature of InSeI tubules. In the image, the chains appear as twisted tubules. The FFT of the HRTEM image can be indexed close to the [011] zone axis, and the representative structure is shown in Figure 1d, right. Comparison of the oriented structure and the HRTEM insinuates that the Zcontrast mainly comes from the heavy iodine atoms in the InSeI tubule.

2.2. Temperature-Dependent Optical Properties of InSel

Thermal stability, another critical property of materials for thermometry, was probed using thermogravimetric analysis (TGA). The TGA curve of InSeI, shown in Figure S4 of the Supporting Information, displays two distinct transitions at 396 °C (669.15 K) and 615 °C (888.15 K), indicating two phase transitions or decomposition pathways. The first transition is sharp and leads to a mass percent decrease of 40%, equivalent to the loss of one stoichiometric equivalent of iodine. Meanwhile, the second transition is broad, and is not equivalent to the loss of 1 stoichiometric equivalent of Se or In. A possible explanation is the formation of In-rich phases from the loss of Se, the more volatile element. The thermal stability of InSeI up to 396 °C (669.15 K) reinforces its case for thermometry applications. Altogether, the structural and physical characterization of InSeI stresses its two most important unique qualities: the highly anisotropic tubular structure

and the thermal stability, which are essential in elaborating the chemistry behind the thermochromism of InSeI.

Investigating the temperature dependence of electronic transitions can lead to the identification of pertinent indicators of the chemical bonding and electronic states of semiconducting crystals. Given that InSeI has a unique 1D structure, determining the temperature dependence of the optical gap can illuminate the relationship between structural anisotropy and optical/electronic properties at a fundamental level. To do so, we measured the optical absorption spectra of InSeI single crystals under inert gas flow across different temperatures. We observe that there is a clear, pronounced, and reversible change in the color of the crystals from beige-colored to yellow to red-orange as the temperature is increased from 93 to 473 K (Figure 2a,b). This systematic trend is also observed in the temperature-dependent absorbance spectra shown in Figure 2c, where the optical band edge undergoes a consistent red shift with increasing temperature. From these spectra, the optical bandgap of InSeI at each temperature was calculated using the Tauc equation, with $\gamma = \frac{1}{2}$. This assignment was based on several first-principles calculations, as well as our own (Figure S6, Supporting Information), that predict a direct gap at the Γ -point of InSeI. [51] Based on the temperature dependence of the optical bandgap (Figure 2d), we demonstrate a large energy range that is accessible from 93 to 473 K, indicating that InSeI exhibits strong thermochromic behavior. The lowering of the optical gap with temperature is a common feature of conventional covalent semiconductors and originates from lattice expansion and phononic contributions.[52]

The first step in determining the major contributor to strong thermochromic behavior in InSeI is fitting the raw data to the O'Donnell–Chen equation using least-squares analysis. The O'Donnell–Chen equation (Equation (1)) is based on a vibronic model and takes into account the phonon contribution to the temperature-dependence of the bandgap

$$E = E_0 - S\langle \hbar \omega \rangle \left[\coth \left(\frac{\langle \hbar \omega \rangle}{2k_{\rm p}T} \right) - 1 \right]$$
 (1)

In this model, the bandgap is a function of a dimensionless coupling constant (S), the average phonon energy ($\langle \bar{h}\omega \rangle$), and temperature. The E_0 value, which approximates the fundamental limit of the optical gap at 0 K, is 2.73 eV, setting the higher end of the wavelength nearing yellow-green color. The calculated $\langle \bar{h}\omega \rangle$ value of average phonon energy is 147 cm⁻¹, which is consistent with the subsequent Raman measurements discussed in the next sections. Strikingly, a rather large S-value (7.32) is calculated for InSeI, pointing to a large correlation between the optical bandgap and temperature.

The maximum slope of the temperature-dependent optical bandgap can be quantified to assess the sensitivity of the bandgap to temperature changes. This term, $(dE_g/dT)_{max}$, is a crucial parameter in identifying thermochromic materials for temperature sensing applications. It is directly related to the thermoptic coefficient^[54] and is calculated from S using the equation, $(dE_g/dT)_{max} = -2Sk$, where k is the Boltzmann's constant. We calculate the $(dE_g/dT)_{max}$ for InSeI to be 1.26×10^{-3} eV K⁻¹, which is relatively large (highly negative) compared to many conventional semiconductors. The $(dE_g/dT)_{max}$ term is composed of two terms: $(dE_g/dT)_{TE}$, which accounts for lattice expansion, and

15214095, 0, Downloaded from https://onlinelibrary.wiley.com/doi/10.1002/adma.202312597 by University Of California - Irvine, Wiley Online Library on [14/05/2024]. See the Term

ons) on Wiley Online Library for rules of use; OA articles are governed by the applicable Creative Commons License

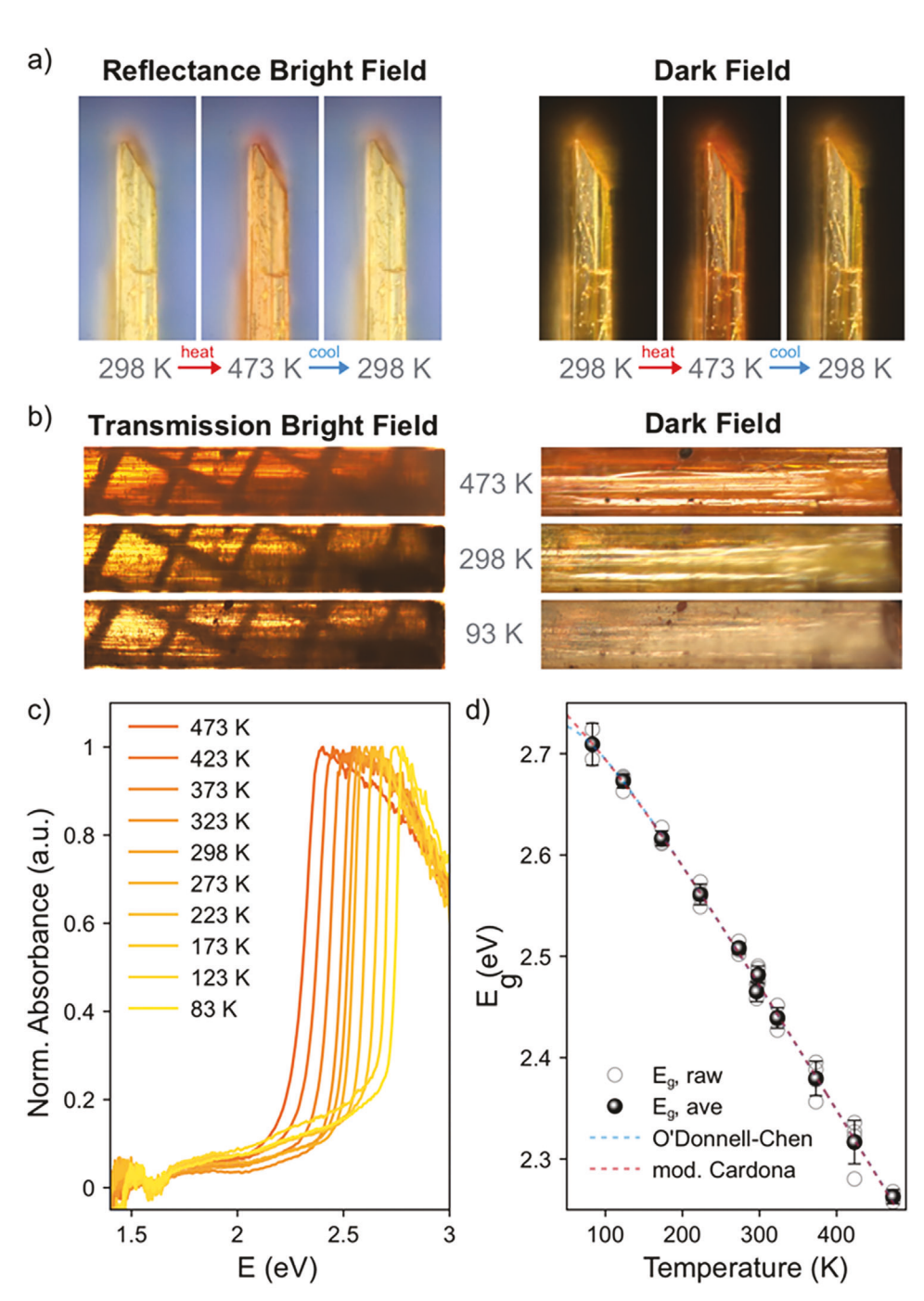


Figure 2. Temperature-dependent optical response of single crystalline InSel. a) Bright- and dark-field optical images of InSel single crystals on SiO_2/Si substrate collected during one heating and cooling cycle from 298 to 473 K. b) Bright- and dark-field optical images of InSel single crystals collected at three distinct temperatures within the investigated range. The crystal under study is mounted on a Cu mesh grid. c) Normalized temperature-dependent absorbance spectra of InSel. d) Relationship of the extrapolated optical direct gap (E_g) of InSel with temperature. The plot also includes the result of least squares fitting to the O'Donnell–Chen and the modified Cardona equation.

 $(dE_{\rm g}/dT)_{\rm EP}$, which accounts for electron–phonon coupling. [55] We then took a semiempirical approach to qualitatively estimate the lattice expansion term by calculating the bandgap of the refined InSeI crystal structures collected at 83 and 298 K using density functional theory (DFT). Because of the small temperature-induced modulation the unit cell dimensions and the asymmetric

unit, there are only minute changes in the overall calculated electronic band structure. At the Γ -point where the direct gap lies, a slight increase in bandgap (+0.033 eV) is expected from the electronic band structures in Figure S6c of the Supporting Information, which contradicts the more pronounced bandgap lowering (-0.24 eV) observed in the temperature-dependent absorbance



www.advmat.de

experiments in the same temperature range. This comparison implies that the thermal expansion increases the gap, which is suggestive that the overall bandgap lowering is not structural in origin but, rather, largely driven by electron-phonon interactions. We then performed an Urbach analysis, shown in Figure S5 of the Supporting Information, on the absorption band edges to determine if static disorder plays a role in the broadening. Analysis of the Urbach tails and the extracted steepness parameters implies that the band edge broadening originates from electronphonon coupling and not from static disorder that may develop at high temperatures. We elaborate on this analysis in Section S1 of the Supporting Information. Our comprehensive fitting and analysis of the optical bandgap data suggests a strong electronphonon coupling effect, however, we cannot discount the possible contribution of purely static structural effects on the electronic structure, which have been observed in soft materials like perovskites.[24,56]

2.3. Investigating Structural Origins of Thermochromism

Thermochromism arising from structural distortions can vary in extent; it can be very strong and abrupt in the case of phase transitions, or weak and continuous, in the case of lattice anharmonicity or electron-phonon coupling. [57] To assess the static structural effect on thermochromism, we compared the refined structure of InSeI using SC-XRD performed on the same crystal at 83 and 298 K. In the temperature range studied, the space group of InSeI ($I4_1/a$) remained the same, but with very minute changes to the atomic positions in the asymmetric unit. At the unit cell level, InSeI undergoes a slight increase in the lattice constants and consequently, unit cell volume (Table S1, Supporting Information). Owing to the prominently vdW nature of InSeI, the changes in the lattice constants are highly anisotropic. We found that the in-plane lattice constant, a, increases by 0.59%, while the out-of-plane lattice constant, *c*, increases only by 0.18%. Calculated coefficients of thermal expansion, α , are comparable to other 1D vdW phases like NbSe₃ and ZrS₃.^[58,59] On the other hand, the axis-dependent changes reflect the anisotropic bonding in the system, as observed in the smaller expansion along the c-axis, which coincides with the crystallographic alignment of the covalent chains.

While there are only subtle changes in the fractional coordinates of the asymmetric unit of InSeI, our more thorough analysis shows that increasing the temperature alters the vdW bonding (intertubule) more than covalent bonding (intratubule) within the unit cell. Compared to conventional semiconductors, in which temperature-induced changes in the bond length scale with temperature, we observe anomalous behavior in the temperature-dependent structure of InSeI. To probe the anomalous temperature-dependent behavior of the individual atomic positions, we compared the room (RT) and low temperature (LT) crystal structures to the "commensurate" room temperature (cRT) crystal structure. For this cRT structure, we modified the LT structure with the RT lattice constants. This is considered the ideal scenario where the atomic positions change proportionally (or commensurately) with the unit cell, since the fractional coordinates are unchanged. Surprisingly, a slight decrease in the [InSe₃I]_n pseudo-tetrahedra volumes is observed upon heating.

The noticeable changes in the coordination environments of the In and Se atoms are summarized in Figure 3a and Table S2 (Supporting Information). The bonds are represented as thick lines while the bond angles are represented as thin lines. The bond color indicates whether there is an increase (red) or decrease (blue) with temperature. Lastly, solid lines indicate that the change is consistent with a commensurate expansion while the dashed lines do not.

In our succeeding analyses, we compared the RT, cRT, and LT structural parameters in Figure 3b-f. The plots show the relative ratios of the RT and cRT parameters with respect to the LT values. Thus, LT values will be equal to 1 and are represented as the dashed line across the x-axis. Points greater than 1 means that there is an increase in the value of the structural feature with increasing temperature and vice versa. Bond lengths shown in Figure 3b, from the RT structure are systematically smaller than their cRT counterparts, indicating that the bonds are shorter than anticipated based on the temperature-induced expansion. Comparing the RT and LT structure also support this assertion, since 60% of the bonds exhibit unexpected shortening, with the In-I bonds undergoing a large bond contraction. From Figure 3c, it can be seen that most bond angles centered at In are smaller than expected while most bond angles centered at Se have the opposite trend. A possible explanation for this trend is the increased repulsion between the iodine and the selenium atoms or the anisotropic nature of the unit cell expansion. The unexpected change in the covalent bond lengths points to equally unexpected behavior of the vdW bonding in the unit cell, represented schematically in Figure 3d and plotted in Figure 3e. Comparing the vdW bond lengths (I-I, Se-I) in the RT and cRT structure, it appears that the values are longer than expected from commensurate expansion. Majority of the vdW bonds increase in length by \approx 1%, considerably larger than any of the changes in the lattice constants, and consequently resulting in an increase in the void space (unfilled volume) of the unit cell at room temperature (Table S2, Supporting Information).

The lengthening of van der Waals bonds at high temperature suggests that the interchain interactions could take a significant part in the thermochromic mechanism of InSeI. To gain insight into this effect, we calculated the interchain interaction energies of the 83 and 298 K structures by comparing ground state energies of a relaxed single chain structure and the relaxed unit cell structures. The interchain interaction energy ($E_{\rm int,ic}$) was calculated using the equation

$$E_{\text{int,ic}} = \frac{E_{\text{unit cell}} - nE_{\text{single chain}}}{N}$$
, where $n = 4$ and $N = 8$ (2)

where n is the number of chains in a unit cell, and N is the number of neighboring chains of each single chain. The calculated energy values obtained from this strategy are summarized in Table S4 of the Supporting Information. The difference between the interchain interaction energies of the 83 and 298 K structures is 0.0176 eV, less than the kinetic energy at ambient conditions, 3/2kT = 0.0259 eV. This minute energy difference suggests that there is a negligible change in the interchain interaction energies when InSeI is heated from 83 to 298 K. Furthermore, we explored the extreme situation where the interchain interaction energy is reduced all the way to zero by calculating the band structure of

SCIENCE NEWS _______ MATERIAL www.advancedsciencenews.com www.advmat.

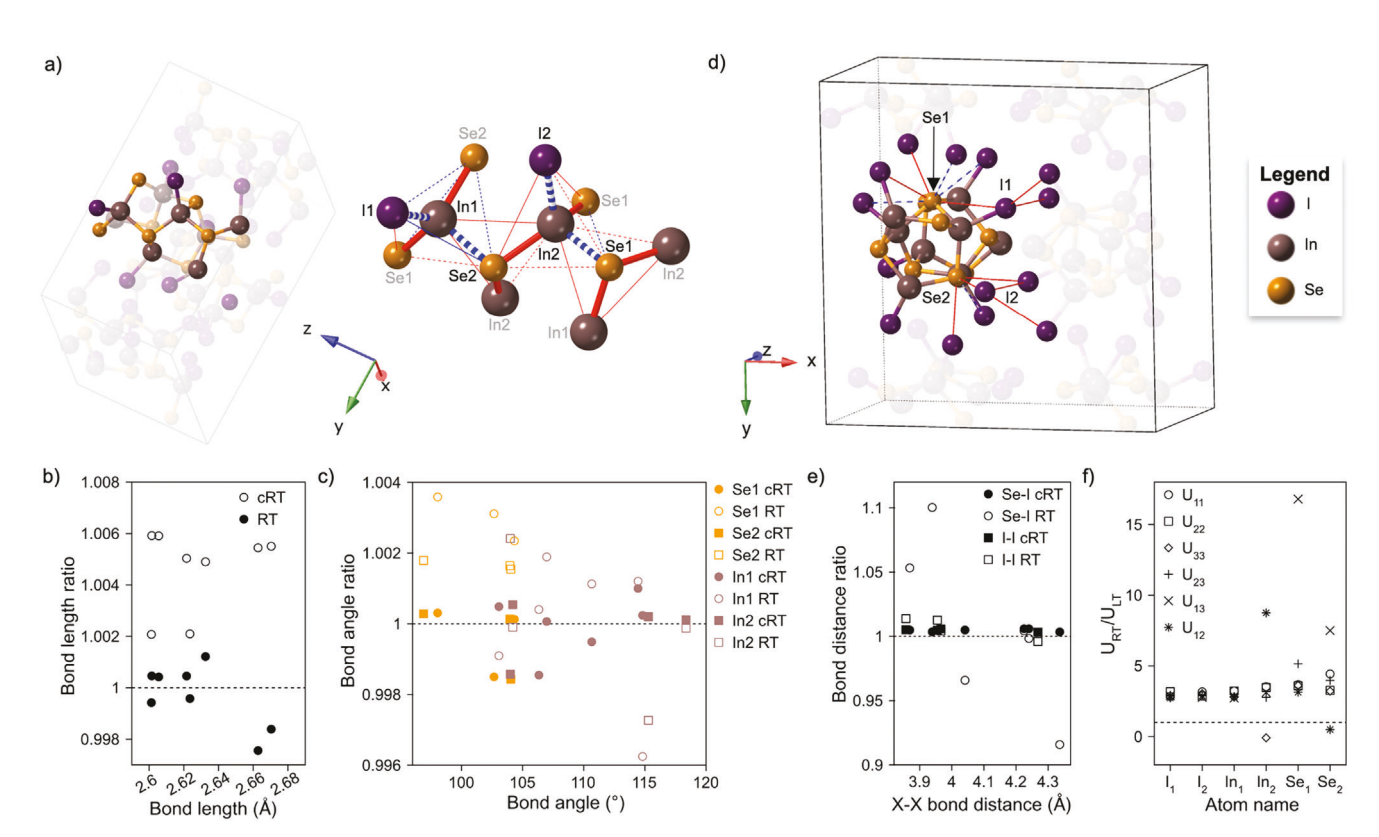


Figure 3. Comparison of the InSel single crystal structure at 83 and 298 K. a) Illustrative summary of the structural changes in the In and Se coordination environment upon temperature increase. (Left panel) Crystal structure representation showing the position of the representative atoms shown as opaque spheres depicted with respect to the other translucent atoms in the InSel unit cell. (Right panel) The coordination environments of representative In and Se atoms in the unit cell. Atomic labels in black are part of the asymmetric unit, while those in gray are part of the pseudo-tetrahedral coordination unit of the central In atoms. The thick and heavy lines correspond to covalent bonds while the thin lines correspond to bond angles. Red color indicates an increase in value, while blue color indicates a decrease in value with increasing temperature. Solid lines indicate a change consistent with the expected commensurate room temperature structure, and dashed lines indicate an opposite trend. b) Bond length ratios of the room temperature (RT) and commensurate room temperature (cRT) structures with respect to the low temperature (LT) structure and depicted as a function of LT bond lengths. c) Ratios of the bond angles corresponding to the RT and cRT structures with respect to the LT structure and depicted as a function of LT bond angle. d) Crystal structure representation of the Se—I and I—I nearest neighbor inter- and intratubule distances, shown as thin lines. These distances are described in the same manner as in (a). The representative atoms of interest are depicted as opaque spheres and the other atoms in the unit cell are shown as translucent spheres. e) X—X bond distance ratios in the RT and cRT structures with respect to the LT structure and depicted as a function of the LT bond distances. f) Mean square displacement, U_{NY}, ratios in the RT structure with respect to the LT structure shown for all atoms in asymmetric unit.

a single chain. In Figure S4 of the Supporting Information, the direct gap of a single chain becomes larger (2.47 eV) compared to the calculated bulk unit cell. From our calculations, the scale of the change in interchain interaction energies at the experimental temperature range is almost negligible, but when the interchain interactions are removed in its entirety, the bandgap increases. This finding suggests that modulating interchain interactions with temperature requires a high trivial temperature to do so, and shifts the gap opposite of the observed experimental trends. Overall, the variable temperature SC-XRD studies suggest that with increasing temperature, the InSeI intrachain covalent bonds get shorter, while the interchain interactions become longer and weaker. The changes in InSeI structure are equivalent to the individual chains moving apart from each other and becoming more "isolated."

So far, the experimental data do not provide strong evidence for static structure as the origin of thermochromism. Now, we look into the dynamic nature of the structure since InSeI could be subject to strong phonon anharmonicity, as a consequence of the structural anisotropy in low-dimensional materials and the confinement-like effect induced by the expansion. Anharmonicity can be manifested as anisotropic temperature dependence of the mean square relative displacement or the thermal ellipsoids of atoms in a crystal structure. [60,61] We compared the ratios of the Debye-Waller factors (U), also known as the anisotropic displacement parameters, of InSeI at different temperatures in Figure 3f. For all atoms in the unit cell, the diagonal components $(U_{11}, U_{22}, U_{23}, U_{$ U₃₃) increase by approximately the same factor with increasing temperature. In contrast, the off-diagonal components (U₁₂, U₁₃, U₂₃) experience atom-dependent changes with temperature, with the Se atoms having the largest change (up to 17-fold increase in U₁₃). The changes in the Debye–Waller factors suggest that the thermal ellipsoid size increases with temperature, as expected, but undergoes some tilting in the process. Disjointed changes in the Debye-Waller factor indicate that there are anisotropic changes in the electron densities with temperature, further emphasizing the role of anharmonicity in the lattice dynamics of

www.advmat.de

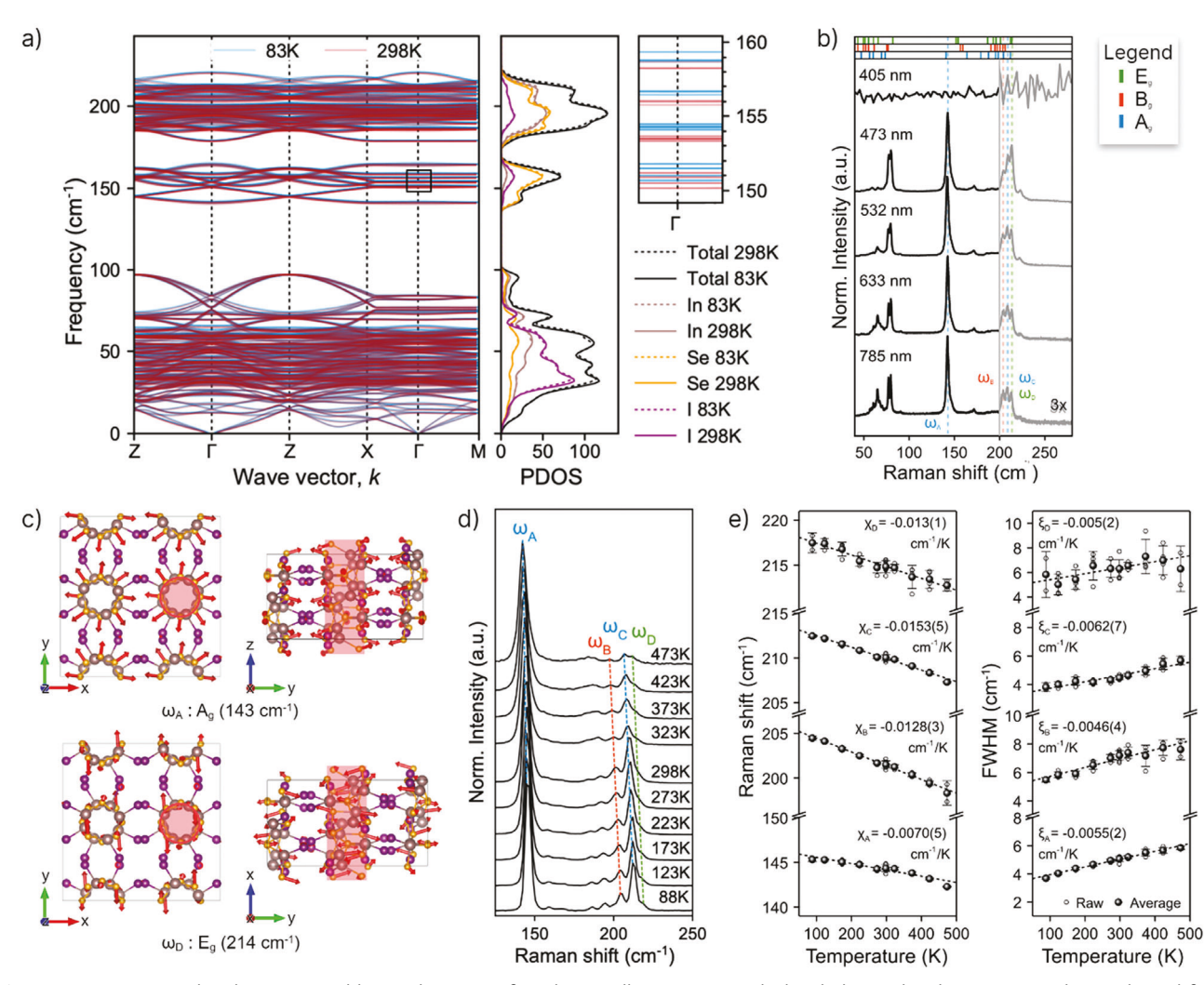


Figure 4. Computational and experimental lattice dynamics of single crystalline InSel. a) Calculated phonon band structures and DOS derived from the experimental InSel single crystal structures at 83 K (blue curves) and 298 K (red curves). b) Stacked room temperature Raman spectra of an InSel crystal measured using different laser excitation wavelengths. The predicted irreducible representations of the Raman-active modes are shown at the top as vertical color-coded bars. Legend: A_g (blue), B_g (orange), and E_g (green). Dashed lines, colors-coding, and positions indicate the assignment of the modes of various representative peaks. c) Phonon displacement diagrams of two representative InSel Raman-active modes. d) Stacked plot of the temperature-dependent Raman spectra measured from a single InSel crystal. The Raman-active mode assignments are labeled and color-coded accordingly. e) Stacked plots of the east squares fitting of the Raman shift frequencies and linewidths (FWHM) with respect to temperature. Dashed lines in (b) and (d) were added as guides to the eye.

We collected laser energy- and temperature-dependent Raman spectroscopy, as well as calculated the phonon density of states to elucidate the role of lattice dynamics on thermochromism. Phonon band structures represent the vibrational modes of the system at absolute zero using the crystal structures at room (298 K) and low temperature (83 K), which were calculated from first-principles using density functional perturbation theory. Based on the point group symmetry of the $I4_1/a$ space group, InSeI is expected have a total of 72 Raman-active modes coming from six occupied 16f Wyckoff sites, and the irreducible representation (I-R), $\Gamma = 18$ $A_{\rm g} + 18$ $B_{\rm g} + 18$ $^1E_{\rm g} + 18$ $^2E_{\rm g}$. The phonon band structures, shown in Figure 4a, contain a total of 288 bands each, coming from the 96-atom unit cell used in the calculation. From the partial phonon density of states (PDOS) of each element (Figure 4a, middle), it is observed that the heavier

iodine atoms have a strong contribution to the lower frequency region (<70 cm $^{-1}$), while the lighter indium and selenium atoms populate the higher frequency regions (>140 cm $^{-1}$). There is an intermediate region with relatively equal contribution from all atoms (70–100 cm $^{-1}$). The total PDOS indicates that there are three energy regimes that vibrational modes occupy; <100 cm $^{-1}$, 130–170 cm $^{-1}$, and 180–220 cm $^{-1}$, each separated by phonon bandgaps. From these first-principles calculations, we assign the sharp peaks observed in the Raman spectra based on the predicted irreducible representations of the phonon modes at and near the Γ point, summarized in Table S5 of the Supporting Information.

Using laser excitation sources of various energies, the Raman spectra of single crystal InSeI were collected at room temperature, shown in Figure 4b, to optimize the ideal conditions for



www.advmat.de

Raman mode assignment. Raman spectra from 785, 633, 473, and 532 nm excitation contain the same number of peaks corresponding to vibrational modes. The Raman spectrum collected with the 405 nm did not express any peaks despite the absence of strong fluorescence background that could obscure the signal. The 532 nm spectrum has significantly higher intensity compared to the other spectra, likely due to resonance Raman effects, as the laser energy (2.33 eV) is close to the optical bandgap (2.45 eV) from the room temperature absorbance measurement in Figure 2b. These conditions were selected as the basis for assigning the Raman mode symmetries because of the high signalto-noise ratio that allows the maximum number of peaks to be fitted accurately. All the predicted Γ -point Raman-active mode frequencies are plotted as bars above the Raman stacked plots in Figure 4b. The large number of phonon modes expected (72 total) within a small spectral range, made it nontrivial to assign the symmetries of the Raman peaks in the frequency region of interest without polarization-orientation experiments. Nonetheless, we were able to assign the strongest peaks that are isolated within the 120-220 cm⁻¹ spectral region. The symmetry assignments were verified by comparing phonon-displaced structures with the original structures using ISODISTORT software. [63,64]

To describe the dynamic nature of these Raman-active modes, we illustrate the phonon displacement diagrams of the assigned modes in Figure 4c, with the exaggerated atom displacement eigenvectors as red arrows. In the unit cells shown in Figure 4c, the outline of the tubule form formed by the In and Se atoms are highlighted in red in order to readily distinguish the relative orientation of the phonon eigenvectors with respect to the tubules. The strongest Raman signal (ω_A), with I-R A_{σ} symmetry, describe the inward and outward vibration of Se atoms with respect to the chain axis, akin to the radial breathing modes of tubular materials like carbon and boron nitride nanotubes.[65] The highest frequency Raman signal (ω_D), with I-R E_{α} symmetry, is associated with the near-lateral vibration of Se atoms along the xy-plane of the unit cell, analogous to the tangential modes in tubular structures.^[66] There are several other vibrational modes that possess the same symmetry as described above, but we focus on those two for their ease in identification among the largely overlapping Raman peaks.

Given the strong phononic contribution to the temperature-dependent optical properties of InSeI, we further investigated lattice dynamics since anharmonic effects are non-negligible at high temperatures. [61] We measured the Raman spectra of InSeI (Figure 4d) at various points within the temperature range, 93–473 K, where thermochromism is observed. In this temperature regime, there are no phase transitions or discontinuities based on the lack of changes in the number of modes (or symmetry) at high and low temperature, which is consistent with the TGA data (Figure S4, Supporting Information) that show that a phase transition only occurs beginning at 396 °C (669.15 K). This is also consistent with the SC-XRD data that show that there are no space group or asymmetric unit change from 83 to 298 K.

From the stacked plot of temperature-dependent Raman spectra in Figure 4d, it is observed that there is a general trend of phonon mode softening and broadening with increasing temperature. Theoretical and experimental studies on low-dimensional materials have reported this behavior as a hall-mark for phonon anharmonicity.^[67,68] The temperature-induced

phonon frequency lowering originates from a combination of lattice volume expansion and anharmonic phonon–phonon interactions. To evaluate these effects, we fitted the temperature-dependent peak frequencies and widths to the linear Grüneisen relationship (Equations (3) and (4))

$$\omega(T) = \omega_0 + \chi(T) \tag{3}$$

$$\Gamma(T) = \Gamma_0 + \xi(T) \tag{4}$$

where χ and ξ are first order coefficients that take into account both the intrinsic contribution of lattice volume expansion and phonon anharmonicity to the frequency red shift and broadening. [60,69,70] Results of the least squares fitting and firstorder coefficient values are summarized in Table S6 of the Supporting Information. On the other hand, the best fit lines, raw data, and temperature-averaged points of the Raman frequencies and linewidths (full-width-at-half-maximum, FWHM) are shown in Figure 4e. We estimate from the calculated PDOS (Figure 4a, right) of the room and low temperature crystal structures that the lattice expansion contribution to frequency softening is 0.7-1.0 cm⁻¹. Hence, this is suggestive that the major factor contributing to the frequency red shift is phonon anharmonicity. From the temperature coefficients, we compared the degree of electron-phonon coupling and anharmonicity of each mode. In general, the higher frequency modes ($\omega_{\rm B}$, $\omega_{\rm C}$, and $\omega_{\rm D}$) have higher coefficients than ω_A , indicating a stronger coupling with electrons. From the PDOS plots, it is observed that these modes have strong In and Se character. Nonetheless, phonons with strong I character, predicted at low frequencies (<100 cm⁻¹), could also play a large role in electron-phonon coupling, because of their high phonon populations even at low temperatures (note that 100 cm⁻¹ is equivalent to 143 K). It is of no surprise that anharmonic modes involving all elements of InSeI drastically alter electronic states, since the CBM has strong I-p character while the VBM has both strong In-s and Se-p character (Figure S6a, Supporting Information).

3. Discussion

Electron-phonon coupling and phonon anharmonicity are closely intertwined in a manner that both are frequently observed simultaneously in many technologically relevant materials. [71–74] Based on our analysis of the temperature-dependent absorbance and Raman data, the large thermochromism of InSeI is a consequence of large bandgap renormalization resulting from both strong electron-phonon coupling and phonon anharmonicity. We propose that the band edge broadening and steepness enlargement is a result of electron-phonon coupling and the disorder introduced by anharmonic phonons. Because the CBM and VBM have strong In, Se, and I orbital character, anharmonic fluctuations will severely alter and smear the band edges, leading to smaller bandgaps.^[75] The same trend has been observed in perovskites, although the opposite trend has been observed as well, suggesting that further work be supported by first-principles calculations that explicitly take into account anharmonicity at finite temperatures.[72,76]

Next, we discuss the possible structural origins of the strong lattice anharmonicity in InSeI. Besides phonon softening and

ADVANCED MATERIALS

www.advmat.de

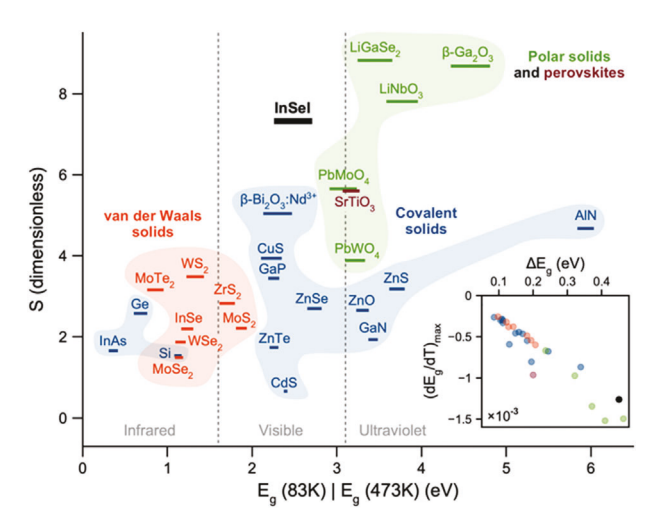


Figure 5. Comparative representation of the thermochromic behavior and electron–phonon coupling strength of InSeI to conventional semiconductors. Relationship of UV–vis–infrared spectral range with extrapolated electron–phonon coupling constant, S, across several known semiconductors and insulators. The inset depicts the relationship of spectral range with respect to calculated $(dE_g/dT)_{max}$ value. $^{[30,81-93]}$

linewidth broadening (FWHM), the lattice anharmonicity was also manifested in the SC-XRD data as anomalous shortening of bond lengths and the tilting of the Se thermal ellipsoids with temperature. The behavior described can be ascribed to the unique aspects of the InSeI structure: the highly anisotropic 1D structure and the tubular geometry of the chains. Anharmonicity in low-dimensional materials is strongly correlated to the way lattice vibrations can dynamically alter atomic interactions within the covalent subunits and across the vdW interfaces. Across interfaces, lattice vibrations can facilitate or hinder short range interactions and influence phonon dispersion and transmission. [77–80]

Quasi-1D materials offer an interesting perspective into this effect because these structures essentially consist of subunits that are surrounded by very diverse interfaces owing to the intrinsic anisotropy of the covalently bound chain cross-sections and the packing of these chains. In InSeI, we identified four distinct high symmetry interfaces around each chain, defined by the (100), (010), (110), and (-110) planes. Across these planes, we measured the Se-I and I-I distances that correspond to interchain vdW interactions. There is disproportionate lengthening of these interchain distances with respect to the lattice constants. As the temperature increases, the gap between chains leads to modified (likely diminished) interactions of Se and I with neighboring chain atoms, also reflected in Figure 1d. These interchain interactions are further influenced by the displacements caused by the radial breathing and tangential modes, which have large eigenvector components pointed toward the interfaces within the vdW gaps. Consequently, the atoms experience varying electronic environments as the atoms oscillate around their equilibrium posi-

In order to contextualize the potential of InSeI for thermometric applications, we compared its thermochromic metrics to conventional covalent- and vdW-bound semiconductors and known materials utilized for optical thermometry. In **Figure 5**, the hypothetical energy ranges covered by various solids from

the literature and their S and $(dE_{\alpha}/dT)_{max}$ values are compared with InSeI. We obtained these values by fitting the temperaturedependent optical bandgap data reported in the literature using the O'Donnell-Chen model and subsequently calculating the hypothetical energy range covered from 83 to 298 K, which is the temperature range investigated in this report. The large electronphonon coupling constant, S, of InSeI has two important implications on its optical properties. First, it means that InSeI will also have a large $(dE_g/dT)_{max}$ value, three times compared to GaAs, a material utilized for nanoKelvin-resolution measurement devices.[18] Second, it indicates that the optical bandgap energies of InSeI cover a large range of temperature values. While InSeI does not have as large of S values compared to polaronic materials like LiNbO₃ or β -Ga₂O₃, [82,84,94] it is the combination of the zero Kelvin gap and the electron-phonon coupling constant, S, that underpins its unique quality. Since the zero Kelvin optical gap lies in the middle of the visible spectrum and electronphonon coupling red shifts this energy with increasing temperature, in many technologically relevant temperature ranges, InSeI will exhibit an optical gap in the visible region.

The thermochromic behavior of InSeI persists when the dimensions of the material are reduced to the nanoscale. Atomic force microscopy (AFM) topography maps of representative In-SeI nanoribbons in Figure S7a of the Supporting Information show that single crystals are easily exfoliated into nanoscale units mechanically using tape. Single crystal InSeI is exfoliable to even thinner nanoribbons (down to 5 nm), however, these samples were chosen to maximize the signal-to-noise ratio of the absorbance measurement. Both the 283 and 150 nm thick ribbons exhibit a red shift in the optical bandgap when heated to high temperatures (Figure S7b, Supporting Information), similar to their bulk single crystal counterparts. The optical bandgaps of the nanoribbons determined from Tauc analysis is plotted alongside the bulk optical bandgap O'Donnell-Chen and modified Cardona model trendline in Figure S7c of the Supporting Information. We observe a distinct blue shift in the optical gaps (up to $\approx 0.1 \text{ eV}$) of the nanoribbons with respect to the bulk single crystal. This trend can be explained by the onset of confinement effects at this thickness regime, as predicted by the DFT calculations on the single chain (Figure S6b, Supporting Information). Another possible explanation are the correlated effects of electron-phonon coupling and phonon anharmonicity at the nanoscale. Phonon of low-dimensional solids with symmetries closely associated with van der Waals interactions is known to vary the temperature sensitivity of their energies and lifetimes when reduced to nanoscale subunits.[66] Interestingly enough, most, if not all the Raman modes of InSeI have strong eigenvector components pointing toward the van der Waals gap, emphasizing the unique nature of 1D vdW materials in modulating electron-phonon and phononphonon interactions.

From an applications standpoint, thermochromic devices that integrate InSeI will only require visible light sensing for temperature detection. To nominally illustrate this concept, digital images of single crystal InSeI illuminated by a halogen light source were taken at different temperatures inside the heating stage, seen in Figure S8a of the Supporting Information. Then, the RGB color histograms were extracted from the digital images using a method adapted from thermochromic polymers. [95] From the RGB distribution of pixels in Figure S8b of the Supporting

ADVANCED MATERIALS

www.advmat.de

Information, a distinct trend in the sharpening in the green and blue histograms was observed. With more optimized experiments, it would be feasible to correlate the RGB values to temperature. Broadly, this simple experiment demonstrates how single crystal InSeI can be applied for thermal sensing. To demonstrate the reversibility of InSeI thermochromism, a representative single crystal sample was cycled between 298 and 473 K multiple times. In Figure \$9 of the Supporting Information, it can be observed that there are no significant changes in the optical band edge position and steepness, indicating that there are no static structural changes like large defect formation evolving from the repeated heat treatment. While a small intrinsic defect density may be present in the single crystals, they do not play an important role in dictating the thermochromism. Thermal cycling to 473 K does not result in the formation of new defects because of the reversibility of the thermochromism. Thermally induced defect formation would lead to the retention of the high temperature optical gap upon cooling back to room temperature. In summary, the large electron-phonon coupling imparts a large accessible energy range for the InSeI optical properties, making it ideal for recurring thermal measurements with visible light readout.

4. Conclusion

Overall, we demonstrated the strong thermochromism of InSeI, a 1D vdW solid, as evidenced by the 50 nm red shift (pale yellow to red-orange) of the optical bandgap over a range of 390 K. Analysis of the bandgap temperature dependence and the spectral features of the Urbach edges points to strong electron-phonon coupling as the main driving force for the thermochromism. The strong electron-phonon coupling is further complemented by the anharmonicity of the InSeI vibrational modes, corroborated by temperature-dependent single crystal structure determination and Raman spectroscopy analysis. We propose that the inherent bonding anisotropy and the tubular nature of the InSeI structure enhances phonon anharmonicity because of the highly anisotropic lattice expansion that heavily alters the inter- and intrachain distances upon heating. The calculated $(dE_{\alpha}/dT)_{max}$ value, 1.26×10^{-3} eV K⁻¹, a metric for temperature sensitivity, is larger than most semiconductors that are optically active in the visible region. Based on the thermochromic metrics extracted from the experimental data, its thermal stability, and the known exfoliability of InSeI, it has potential for implementation as solution-processable thermal sensors at both cryogenic and high temperatures, making it suitable for a variety of applications ranging from automotive engine thermal management, cold storage monitoring, and nanothermometry.

Supporting Information

Supporting Information is available from the Wiley Online Library or from the author.

Acknowledgements

This work was primarily supported by the University of California, Irvine (UCI). D.L.M.C. and M.Q.A. acknowledge partial support of the UCI MR-SEC, Center for Complex and Active Materials, under the National Science

Foundation (NSF) (Award No. DMR-2011967). G.M.M. and M.Q.A. acknowledge the NSF Graduate Research Fellowship Program. L.C. acknowledges support from the UCI Quantum Undergraduate Research Opportunities Program. Y.Z. and R.W. were supported by the National Science Foundation Materials Research Science and Engineering Center program through the UC Irvine Center for Complex and Active Materials under Award No. DMR-2011967 and the Department of Energy, Office of Basic Energy Sciences, under Award number DE-FG02-05ER46237. Computer simulations were performed at NERSC. Several aspects of this work were performed at the UC Irvine Materials Research Institute (IMRI). Facilities and instrumentation at IMRI were supported, in part, by NSF through the UCI MRSEC. XPS was performed using instrumentation funded in part by the National Science Foundation Major Research Instrumentation Program under Grant No. CHE-1338173. AFM was performed using an Anton Paar Tosca 400 AFM on loan to IMRI from Anton Paar GmbH. The authors also thank the UC Irvine Department of Chemistry Laser Spectroscopy Labs and its director, Dr. Dmitry Fishman, for instrument support.

Conflict of Interest

The authors declare no conflict of interest.

Data Availability Statement

The data that support the findings of this study are available from the corresponding author upon reasonable request.

Keywords

one-dimensional, thermochromic, van der Waals solid

Received: November 23, 2023 Revised: January 8, 2024 Published online:

- [1] A. E. Dessler, Introduction to Modern Climate Change, Cambridge University Press, Cambridge 2021.
- [2] C. A. Holmquist, W. D. Tiedeman, J. Milk Food Technol. 2019, 1, 11.
- [3] M. Aldén, A. Omrane, M. Richter, G. Särner, Prog. Energy Combust. Sci. 2011, 37, 422.
- [4] G. R. Peacock, AIP Conf. Proc. 2003, 684, 813.
- [5] I. P. Herman, IEEE J. Sel. Top. Quantum Electron. 1995, 1, 1047.
- [6] A. S. Hussain, H. S. Hussain, N. Betcher, R. Behm, B. Cagir, Sci. Rep. 2021, 11, 11832.
- [7] M. R. Moldover, W. L. Tew, H. W. Yoon, Nat. Phys. 2016, 12, 7.
- [8] Y. Huang, J. Pei, P. V. Nielsen, F. Bonthoux, S. Lechene, F. Keller, S. Wu, C. Xu, Z. Cao, in *Industrial Ventilation Design Guidebook*, Academic Press, Cambridge, MA 2021, pp. 185–277.
- [9] N. Klimov, T. Purdy, Z. Ahmed, Sens. Actuators, A 2018, 269, 308.
- [10] Z. Ahmed, N. Klimov, T. P. Purdy, T. Herman, K. Douglass, R. P. Fitzgerald, R. Kundagrami, Photonic Thermometry: Upending 100 Year-Old Paradigm in Temperature Metrology in Proceedins of SPIE Silicon Photonics XIV, Society of Photo-Optical Instrumentation Engineers 2019, 10923.
- [11] T. Briant, S. Krenek, A. Cupertino, F. Loubar, R. Braive, L. Weituschat, D. Ramos, M. J. Martin, P. A. Postigo, A. Casas, R. Eisermann, D. Schmid, S. Tabandeh, O. Hahtela, S. Pourjamal, O. Kozlova, S. Kroker, W. Dickmann, L. Zimmermann, G. Winzer, T. Martel, P. G. Steeneken, R. A. Norte, S. Briaudeau, J. Ocul. Pharmacol. Ther. 2022, 3, 159.



www.advmat.de

- [12] F. Menges, P. Mensch, H. Schmid, H. Riel, A. Stemmer, B. Gotsmann, Nat. Commun. 2016, 7, 10874.
- [13] C. Cressoni, F. Vurro, E. Milan, M. Muccilli, F. Mazzer, M. Gerosa, F. Boschi, A. E. Spinelli, D. Badocco, P. Pastore, N. F. Delgado, M. H. Collado, P. Marzola, A. Speghini, ACS Appl. Mater. Interfaces 2023, 15, 12171
- [14] W. Xu, S. Zong, F. Shang, L. Zheng, Z. Zhang, Photonics Res. 2022, 10, 2532.
- [15] H. Zhou, M. Sharma, O. Berezin, D. Zuckerman, M. Y. Berezin, ChemPhysChem 2016, 17, 27.
- [16] G. Kucsko, P. C. Maurer, N. Y. Yao, M. Kubo, H. J. Noh, P. K. Lo, H. Park, M. D. Lukin, *Nature* 2013, 500, 54.
- [17] P. Bamfield, M. Hutchings, Chromic Phenomena: Technological Applications of Colour Chemistry, Royal Society of Chemistry, London 2018.
- [18] A. Reihani, E. Meyhofer, P. Reddy, Nat. Photonics 2022, 16, 422.
- [19] J. H. Day, Chem. Rev. 1968, 68, 649.
- [20] J. S. Chivian, R. N. Claytor, D. D. Eden, R. B. Hemphill, Appl. Opt. 1972, 11, 2649.
- [21] V. Fernández, F. Jaque, J. M. Calleja, Solid State Commun. 1986, 59, 803.
- [22] W. Ning, X. Zhao, J. Klarbring, S. Bai, F. Ji, F. Wang, S. I. Simak, Y. Tao, X. Ren, L. Zhang, W. Huang, I. A. Abrikosov, F. Gao, Adv. Funct. Mater. 2019, 29, 1807375.
- [23] A. Singh, S. Satapathi, Adv. Opt. Mater. 2021, 9, 2101062.
- [24] J. Lin, M. Lai, L. Dou, C. S. Kley, H. Chen, F. Peng, J. Sun, D. Lu, S. A. Hawks, C. Xie, F. Cui, A. P. Alivisatos, D. T. Limmer, P. Yang, Nat. Mater. 2018, 17, 261.
- [25] J. Troyano, O. Castillo, J. I. Martínez, V. Fernández-Moreira, Y. Ballesteros, D. Maspoch, F. Zamora, S. Delgado, Adv. Funct. Mater. 2018. 28. 1704040.
- [26] S. Mehta, A. Kushwaha, R. R. Kisannagar, D. Gupta, RSC Adv. 2020, 10, 21270.
- [27] W. Zhang, Z. Sun, J. Zhang, S. Han, C. Ji, L. Li, M. Hong, J. Luo, J. Mater. Chem. C 2017, 5, 9967.
- [28] S. W. Allison, Meas. Sci. Technol. 2019, 30, 072001.
- [29] X. Tang, X. Li, Z. Zou, Z. Ma, J. Zhang, Z. Wang, Z. Ci, D. Wang, S. Peng, H. Li, Y. Wang, J. Mater. Chem. C 2017, 5, 10369.
- [30] M. Back, J. Xu, J. Ueda, A. Benedetti, S. Tanabe, Chem. Mater. 2022, 34, 8198.
- [31] K. Song, J. Wang, L. Feng, F. He, Y. Yin, J. Yang, Y. Song, Q. Zhang, X. Ru, Y. Lan, G. Zhang, H. Yao, Angew. Chem., Int. Ed. 2022, 61, 202208960.
- [32] Y. P. Varshni, Physica 1967, 34, 149.
- [33] D. Qiu, F. Huang, S. Li, Q. Mi, Solid State Commun. 2017, 264, 35.
- [34] M. Chaudhary, A. Karmakar, V. Mishra, A. Bhattacharya, D. Mumbaraddi, A. Mar, V. K. Michaelis, Commun. Chem. 2023, 6, 75.
- [35] A. Chaves, J. G. Azadani, H. Alsalman, D. R. da Costa, R. Frisenda, A. J. Chaves, S. H. Song, Y. D. Kim, D. He, J. Zhou, A. Castellanos-Gomez, F. M. Peeters, Z. Liu, C. L. Hinkle, S.-H. Oh, P. D. Ye, S. J. Koester, Y. H. Lee, P. Avouris, X. Wang, T. Low, npj 2D Mater. Appl. 2020, 4, 29.
- [36] Y. Park, C. C. S. Chan, R. A. Taylor, Y. Kim, N. Kim, Y. Jo, S. W. Lee, W. Yang, H. Im, G. Lee, Sci. Rep. 2018, 8, 5380.
- [37] G. Plechinger, A. Castellanos-Gomez, M. Buscema, H. S. J. van der Zant, G. A. Steele, A. Kuc, T. Heine, C. Schüller, T. Korn, 2D Mater. 2015, 2, 015006.
- [38] A. A. Balandin, R. K. Lake, T. T. Salguero, Appl. Phys. Lett. 2022, 121, 040401.
- [39] A. A. Balandin, F. Kargar, T. T. Salguero, R. K. Lake, *Mater. Today* 2022, 55, 74.
- [40] K. H. Choi, S. Cho, B. J. Jeong, B. Lee, J. Jeon, J. Kang, X. Zhang, H.-S. Oh, J.-H. Lee, H. K. Yu, J.-Y. Choi, J. Alloys Compd. 2022, 927, 166995.
- [41] S. Zhao, J. Hu, Z. Zhu, X. Yao, W. Li, Appl. Phys. Lett. 2023, 123, 172404.

- [42] G. Sawitzki, D. Müller, H. Hahn, Mater. Res. Bull. 1980, 15, 753.
- [43] R. Kniep, A. Wilms, J. Beister, K. Syassen, Z. Naturforsch., B: J. Chem. Sci. 1981, 36, 1520.
- [44] D. L. M. Cordova, D. C. Johnson, ChemPhysChem 2020, 21, 1345.
- [45] L. F. Voss, J. W. Murphy, Q. Shao, R. A. Henderson, C. D. Frye, M. A. Stoyer, R. J. Nikolic, *Appl. Phys. Lett.* 2018, 113, 242103.
- [46] C. D. Wanger, W. M. Riggs, L. E. Davis, J. F. Moulder, G. E. Muilenberg, Handbook of X-Ray Photoelectron Spectroscopy, Perkin-Elmer Corp., Physical Electronics Division, Eden Prairie, MN 1979.
- [47] B. H. Freeland, J. J. Habeeb, D. G. Tuck, Can. J. Chem. 1977, 55, 1527.
- [48] H. Henck, D. Pierucci, J. Zribi, F. Bisti, E. Papalazarou, J.-C. Girard, J. Chaste, F. Bertran, P. L. Fèvre, F. Sirotti, L. Perfetti, C. Giorgetti, A. Shukla, J. E. Rault, A. Ouerghi, *Phys. Rev. Mater.* 2019, 3, 034004.
- [49] J. F. Moulder, W. F. Stickle, P. E. Sobol, K. D. Bomben, Handbook of X-Ray Photoelectron Spectroscopy, Perkin-Elmer Corporation, Physical Electronics Division, Eden Prairie, MN 1992.
- [50] P. Makuła, M. Pacia, W. Macyk, J. Phys. Chem. Lett. 2018, 9, 6814.
- [51] S. Jiang, H. Yin, G.-P. Zheng, B. Wang, S. Guan, B.-J. Yao, Phys. Chem. Chem. Phys. 2020, 22, 27441.
- [52] Y. Zhang, Z. Wang, J. Xi, J. Yang, J. Phys.: Condens. Matter 2020, 32, 475503.
- [53] K. P. O'Donnell, X. Chen, Appl. Phys. Lett. 1991, 58, 2924.
- [54] J. Wei, J. M. Murray, J. Barnes, L. P. Gonzalez, S. Guha, J. Electron. Mater. 2012, 41, 2857.
- [55] A. Francisco-López, B. Charles, O. J. Weber, M. I. Alonso, M. Garriga, M. Campoy-Quiles, M. T. Weller, A. R. Goñi, J. Phys. Chem. Lett. 2019, 10, 2971.
- [56] A. Elattar, H. Suzuki, R. Mishima, K. Nakao, H. Ota, T. Nishikawa, H. Inoue, A. K. K. Kyaw, Y. Hayashi, J. Mater. Chem. C 2021, 9, 3264.
- [57] P. Kiria, G. Hyett, R. Binions, Adv. Mater. Lett. 2010, 1, 86.
- [58] J. L. Hodeau, M. Marezio, C. Roucau, R. Ayroles, A. Meerschaut, J. Rouxel, P. Monceau, J. Phys. C: Solid State Phys. 2001, 11, 4117.
- [59] K. Giagloglou, J. L. Payne, C. Crouch, R. K. B. Gover, P. A. Connor, J. T. S. Irvine, J. Electrochem. Soc. 2016, 163, A3126.
- [60] P. Wu, F.-R. Fan, M. Hagihala, M. Kofu, K. Peng, Y. Ishikawa, S. Lee, T. Honda, M. Yonemura, K. Ikeda, T. Otomo, G. Wang, K. Nakajima, Z. Sun, T. Kamiyama, New J. Phys. 2020, 22, 083083.
- [61] B. Wei, Q. Sun, C. Li, J. Hong, Sci. China: Phys., Mech. Astron. 2021, 64, 117001.
- [62] G. Batignani, G. Fumero, A. R. S. Kandada, G. Cerullo, M. Gandini, C. Ferrante, A. Petrozza, T. Scopigno, Nat. Commun. 2018, 9, 1971
- [63] J. Maultzsch, H. Telg, S. Reich, C. Thomsen, Phys. Rev. B 2005, 72, 205438.
- [64] R. Chowdhury, C. Y. Wang, S. Adhikari, F. Scarpa, Nanotechnology 2010, 21, 365702.
- [65] L. Wirtz, A. Rubio, 2009, 105.
- [66] S. Paul, S. Karak, A. Mathew, A. Ram, S. Saha, Phys. Rev. B 2021, 104, 075418.
- [67] L. Xu, W. Wang, Q. Xie, C. Hu, L. Chen, J. Zheng, H. Yin, G. Cheng, X. Ai, J. Raman Spectrosc. 2022, 53, 104.
- [68] X. Yan, B. Wang, Y. Hai, D. R. Kripalani, Q. Ke, Y. Cai, Sci. China: Phys., Mech. Astron. 2022, 65, 117004.
- [69] T. Baikie, N. S. Barrow, Y. Fang, P. J. Keenan, P. R. Slater, R. O. Piltz, M. Gutmann, S. G. Mhaisalkar, T. J. White, J. Mater. Chem. A 2015, 3, 9298.
- [70] L. Hu, J. Chen, A. Sanson, H. Wu, C. G. Rodriguez, L. Olivi, Y. Ren, L. Fan, J. Deng, X. Xing, J. Am. Chem. Soc. 2016, 138, 8320.
- [71] F. Wang, W. Chu, L. Huber, T. Tu, Y. Dai, J. Wang, H. Peng, J. Zhao, X.-Y. Zhu, Proc. Natl. Acad. Sci. USA 2022, 119, 2122436119.
- [72] Y.-N. Wu, W. A. Saidi, J. K. Wuenschell, T. Tadano, P. Ohodnicki, B. Chorpening, Y. Duan, J. Phys. Chem. Lett. 2020, 11, 2518.
- [73] B. Zhang, J. Klarbring, F. Ji, S. I. Simak, I. A. Abrikosov, F. Gao, G. Y. Rudko, W. M. Chen, I. A. Buyanova, J. Phys. Chem. C 2023, 127, 1908.



www.advmat.de

- [74] P. Zhang, Y. Xue, P. Dev, Solid State Commun. 2008, 148, 151.
- [75] M. V. Kurik, Phys. Status Solidi 1971, 8, 9.
- [76] S. A. Seidl, X. Zhu, G. Reuveni, S. Aharon, C. Gehrmann, S. Caicedo-Dávila, O. Yaffe, D. A. Egger, Phys. Rev. Mater. 2023, 7, L092401.
- [77] A. A. Balandin, D. L. Nika, Mater. Today 2012, 15, 266.
- [78] X. Xu, J. Chen, B. Li, J. Phys.: Condens. Matter 2016, 28, 483001.
- [79] S.-Y. Yue, R. Yang, B. Liao, Phys. Rev. B 2019, 100, 115408.
- [80] V. G. Plekhanov, Springer Ser. Mater. Sci. 2018, 53.
- [81] A. Yelisseyev, F. Liang, L. Isaenko, S. Lobanov, A. Goloshumova, Z. S. Lin, Opt. Mater. 2017, 72, 795.
- [82] A. R. Zanatta, Res. Phys. 2022, 39, 105736.
- [83] M. Isik, N. M. Gasanly, N. H. Darvishov, V. E. Bagiev, Phys. Scr. 2022, 97, 045803.
- [84] L. Cheng, Y. Zhu, W. Wang, W. Zheng, J. Phys. Chem. Lett. 2022, 13, 3053.
- [85] D. J. Kok, K. Irmscher, M. Naumann, C. Guguschev, Z. Galazka, R. Uecker, Phys. Status Solidi 2015, 212, 1880.
- [86] M. Isik, N. M. Gasanly, Mater. Sci. Semicond. Process. 2020, 107, 104862.

- [87] M. Moustafa, A. Wasnick, C. Janowitz, R. Manzke, Phys. Rev. B 2017, 95, 245207.
- [88] J. Kopaczek, S. Zelewski, K. Yumigeta, R. Sailus, S. Tongay, R. Kudrawiec, J. Phys. Chem. C 2022, 126, 5665.
- [89] M. Isik, H. H. Gullu, S. Delice, M. Parlak, N. M. Gasanly, Mater. Sci. Semicond. Process. 2019, 93, 148.
- [90] M. Isik, N. M. Gasanly, N. H. Darvishov, V. E. Bagiev, Opt. Mater. 2022, 126, 112210.
- [91] H. H. Gullu, M. Isik, N. M. Gasanly, M. Parlak, *Phys. Scr.* **2020**, *95*, 075804
- [92] M. Bhowmick, H. Xi, M. Androulidaki, B. Ullrich, Phys. Scr. 2019, 94, 085701.
- [93] P. Geng, W. Li, X. Zhang, X. Zhang, Y. Deng, H. Kou, J. Phys. D: Appl. Phys. 2017, 50, 40LT02.
- [94] S. Yamaoka, M. Nakayama, Phys. Status Solidi C 2016, 13, 93.
- [95] S. Lim, D. L. M. Cordova, A. S. Robang, Y. Kuang, K. S. Ogura, A. K. Paravastu, M. Q. Arguilla, H. A. M. Ardoña, *Biomacromolecules* 2023, 24, 4051.